



Article scientifique

Article

2022

Published version

Open Access

This is the published version of the publication, made available in accordance with the publisher's policy.

Controlling the Defects of Cs₂AgBiBr₆ by Varied Precursor Compositions

Frebel, Alexander; Yoon, Songhak; Meles Neguse, Samuel; Jöckel, Dennis M.; Widenmeyer, Marc; Lange, Stefan; Naumann, Volker; Rosspeintner, Arnulf; Ebbinghaus, Stefan G.; Balke, Benjamin; Weidenkaff, Anke

How to cite

FREBEL, Alexander et al. Controlling the Defects of Cs₂AgBiBr₆ by Varied Precursor Compositions. In: Advanced photonics research, 2022, vol. 3, n° 11, p. 2200061. doi: 10.1002/adpr.202200061

This publication URL: <https://archive-ouverte.unige.ch/unige:182138>

Publication DOI: [10.1002/adpr.202200061](https://doi.org/10.1002/adpr.202200061)

© The author(s). This work is licensed under a Creative Commons Attribution (CC BY 4.0)

<https://creativecommons.org/licenses/by/4.0>

Controlling the Defects of Cs₂AgBiBr₆ by Varied Precursor Compositions

Alexander Frebel, Songhak Yoon,* Samuel Meles Neguse, Dennis M. Jöckel, Marc Widenmeyer, Stefan Lange, Volker Naumann, Arnulf Rosspeintner, Stefan G. Ebbinghaus, Benjamin Balke, and Anke Weidenkaff

The amount and type of defects in Cs₂AgBiBr₆ are controlled by varying the Ag/Bi ratio of the precursor solutions in two different synthesis routes, that is, slow solution cooling crystallization and fast microwave-assisted hydrothermal synthesis. The correlation between the Ag/Bi ratio in the precursor solution and defect formation in the crystals is studied by band broadening analysis in Raman spectroscopy, the estimated Urbach energy in UV-vis spectroscopy, and thermogravimetric analysis. Ag-rich precursors are found to prevent the formation of the secondary-phase Cs₃Bi₂Br₉, but at the same time induced the formation of Br vacancies and antisite defects. Time-resolved photoluminescence measurements reveal that the formation of beneficial defects such as Br vacancies causes to trap the charge carriers, thus avoiding the recombination of charge carriers and leading to a longer carrier lifetime. Herein, the findings provide a guidance to decrease the defect densities and can be applied to the fabrication of Pb-free solar cells based on Cs₂AgBiBr₆.

1. Introduction

Because of their outstanding optoelectronic properties, organic-inorganic metal halide perovskites are one of the most intensely studied materials. In the research field of photovoltaic (PV) cells, the presence of the toxic element Pb is considered as one of the main obstacles together with stability issues.^[1,2] As a Pb-free alternative Cs₂AgBiBr₆ is thoroughly investigated being a promising candidate for PV application.^[3–7] The power conversion efficiency (PCE) of Cs₂AgBiBr₆ was reported to be as high as 3.11%.^[8] Previous reports of lower PCE in Cs₂AgBiBr₆-based perovskite solar cell mostly resulted from the induced defects, which act as trap states leading to a low external quantum efficiency (EQE) and

photoluminescence quantum yield (PLQY).^[9–11] For instance, the majority of carriers (>99%) was found to decay through a fast trapping process^[12–14] and the PLQY was reported to be as low as 0.084%.^[15] The generated defects in Cs₂AgBiBr₆ were found to act as non-radiative recombination centers, hampering the process of charge transfer.^[16] Thus, the carrier lifetime and EQE of Cs₂AgBiBr₆ need to be improved to enhance the PCE, and one of the major challenges is a fundamental understanding of the defect formation in Cs₂AgBiBr₆.^[15]

The optical properties of Cs₂AgBiBr₆ are tunable by varying the synthesis conditions such as temperature, pressure, cooling rate for nucleation and crystal growth, or precursor stoichiometry. Many researchers have also evidenced that the composition and crystallinity of Cs₂AgBiBr₆ single crystals are strongly dependent on the synthesis route. Understandably, Ag-rich precursor conditions are reported to be favorable for preventing the formation of Ag vacancies.^[17–20] Furthermore, the ordering and arrangement of the Ag and Bi octahedra, which influence the optical properties of Cs₂AgBiBr₆, are affected by the synthesis conditions as well.^[21,22] C.W. Ahn et al. have recently shown that by controlling the Ag/Bi ratio in hydrothermal synthesis, the formation of Ag vacancies and the subsequent secondary-phase Cs₃Bi₂Br₉ can be avoided. In addition, they found a critical parameter for the initial chemical reaction (nucleation), crystallization, and resulting defect formation in Cs₂AgBiBr₆ single crystal growth.^[17] However, the previously investigated initial Ag/Bi ratio was rather narrow, ranging from 1:1.2 to 1.2:1. Thus, it is of special interest to investigate the effect of the Ag⁺ and Bi³⁺

A. Frebel, S. Yoon, S. Meles Neguse, D. M. Jöckel, B. Balke, A. Weidenkaff
Energy Materials
Fraunhofer Research Institution for Materials Recycling and Resource
Strategies IWKS
Aschaffener Strasse 121, 63457 Hanau, Germany
E-mail: song.hak.yoon@iwks.fraunhofer.de

M. Widenmeyer, A. Weidenkaff
Institute of Materials Science, Research Division Materials and Resources
Technical University of Darmstadt
Alarich-Weiss-Strasse 2, 64287 Darmstadt, Germany

S. Lange, V. Naumann
Diagnostics and Metrology
Fraunhofer CSP Center for Silicon Photovoltaics
Otto-Eißfeldt-Strasse 12, 06120 Halle (Saale), Germany

A. Rosspeintner
Department of Physical Chemistry
University of Geneva
Quai Ernest Ansermet 30, CH-1211 Geneva 4, Switzerland

S. G. Ebbinghaus
Institute of Chemistry
Martin Luther University Halle-Wittenberg
Kurt-Mothes-Strasse 2, 06120 Halle (Saale), Germany

 The ORCID identification number(s) for the author(s) of this article can be found under <https://doi.org/10.1002/adpr.202200061>.

© 2022 The Authors. Advanced Photonics Research published by Wiley-VCH GmbH. This is an open access article under the terms of the Creative Commons Attribution License, which permits use, distribution and reproduction in any medium, provided the original work is properly cited.

DOI: 10.1002/adpr.202200061

concentration in a broader range, which is expected to result in $\text{Cs}_2\text{AgBiBr}_6$ single crystals with different types and concentrations of defects.

In this work, varying precursor compositions were used in two different synthesis approaches, that is, slow solution cooling and fast microwave-assisted hydrothermal synthesis with the aim of systematically controlling the amount and type of defects in the obtained crystals. The change of defect concentrations is confirmed by Raman and UV-vis spectroscopy. The charge-carrier dynamics are investigated by time-resolved photoluminescence (TR-PL). Our findings provide a strategic guidance to decrease the detrimental defects in $\text{Cs}_2\text{AgBiBr}_6$ and can thus be applied to the fabrication of Pb-free inorganic solar cells.

2. Experimental Section

2.1. Synthesis of $\text{Cs}_2\text{AgBiBr}_6$ Crystals

The $\text{Cs}_2\text{AgBiBr}_6$ crystals were prepared by two different wet chemical routes, namely solution cooling in an oil bath and microwave-assisted hydrothermal synthesis in a microwave digestion system (Turbowave 1500, MLS). CsBr (99.9%, metal basis, Alfa Aesar), AgBr (99.5%, Alfa Aesar), BiBr_3 (99%, Alfa Aesar), and aqueous HBr solution (48%, Alfa Aesar) were used as chemicals. For the solution cooling method in each batch 12 mL HBr solution was used to obtain the target amount of 1 mmol $\text{Cs}_2\text{AgBiBr}_6$. Five samples were prepared with varying AgBr to BiBr_3 ratio. The corresponding amounts of precursors used are listed in Table S1, Supporting Information. The oil bath was heated to 110 °C on a hot plate and the reaction vessels were

sealed to prevent evaporation of the solvent. After complete dissolution of the starting chemicals, the hot solutions were slowly cooled down to room temperature at a rate of 5 °C h⁻¹. The obtained crystals were dried and stored in air. In the following, the corresponding samples were denoted as SC_Bi25, SC_Bi33, SC_Bi50, SC_Bi66, and SC_Bi75, respectively. For the microwave-assisted hydrothermal synthesis, the precursor solutions were prepared with the same concentrations as in the solution cooling method. The starting precursors together with HBr solution were placed in a Teflon-lined autoclave and heated in the microwave system to 200 °C within 10 min with a pressure of 4.7 MPa and kept at this temperature for a dwell time of 1 h. The solutions were cooled down to 50 °C with a rate of 150 °C h⁻¹. The obtained samples are denoted in the following as MH_Bi25, MH_Bi33, MH_Bi50, MH_Bi66, and MH_Bi75, respectively. Both solution cooling method and the microwave-assisted hydrothermal method are schematically shown in Figure 1.

2.2. Characterization of $\text{Cs}_2\text{AgBiBr}_6$ Crystals

Raman spectra were obtained at room temperature using a Bruker SENTERRA Raman microscope equipped with a He-Ne laser (wavelength of 632.8 nm; laser power of 20 mW) with a resolution of 2–5 cm⁻¹. An objective lens with a magnification of 20 and an aperture of 25 μm was chosen. The same microscope was also used to take optical images of the crystals. The crystallites size, their distribution, and their morphology were studied by Zeiss Merlin field-emission scanning electron microscope (SEM) operating at 8 kV. Single-crystal X-ray diffraction (XRD) was carried out at room temperature on a STOE IPDS-2 T imaging plate diffractometer (Mo-K_α, graphite

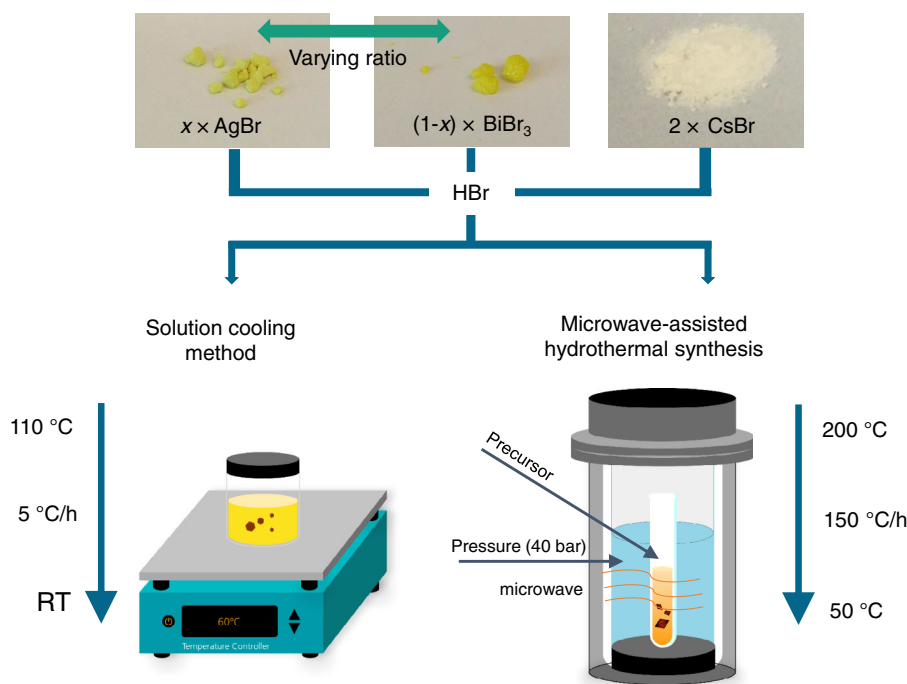


Figure 1. Schematic illustration of the two synthesis routes: Solution cooling method (left) and microwave-assisted hydrothermal synthesis (right).

monochromator, 5 min frame⁻¹, $\omega = 0^\circ$ – 180° , $2\theta_{\max} = 60^\circ$). The crystal structure refinements were carried out with the program ShelXL. Due to the high-absorption coefficient for Cs₂AgBiBr₆, a numerical absorption correction was carried out based on the observed crystal shapes, which were modified using the STOE XShape tool by minimizing the deviations of the intensities of symmetry equivalent reflections. The optical absorption spectra of the samples were investigated using a Perkin Elmer Lambda 900 spectrometer equipped with a deuterium arc lamp for UV light and a tungsten–halogen lamp for visible and near-infrared light. The baseline measurement was taken with BaSO₄. The diffuse reflectance measurements were conducted with a scan speed of 500 nm min⁻¹ in the wavelength range from 1000 to 200 nm. The obtained reflectance spectra were converted to absorbance by using the Kubelka–Munk function $F(R)$ (Equation (1)).

$$a \approx F(R) = \frac{(1 - R)^2}{2R} \quad (1)$$

where a is the absorbance and R is the measured reflectance.^[23] Using the Tauc plot method, the bandgaps were determined.^[24] In addition, the Urbach energy was determined from the obtained absorption spectra, which was interpreted as one of the indicators for crystal imperfection and defects.^[25] For the determination of the Urbach energy E_U , the absorbance was plotted versus the photon energy (Equation (2)).

$$\alpha(E) = \alpha_0 \exp\left(\frac{hv}{E_U}\right) \quad (2)$$

X-ray photoelectron spectroscopy (XPS) was performed in a Kratos Axis Ultra DLD instrument, equipped with a monochromatic Al-K α source ($E = 1486.6$ eV). An analysis area of $300 \times 700 \mu\text{m}$ was defined by an electrostatic–magnetic lens system. Sample charging was suppressed by a low-energy electron flood gun. Survey spectra in the binding energy range between 1330 and 5 eV binding energy were recorded with an analyzer pass energy (PE) of 80 and 0.5 eV step width. Core level and valence band detail spectra were recorded with a PE of 10 eV and energy step width of 0.1 and 0.025 eV, respectively. For acquisition of elemental information at depths larger than the information depth of XPS (few nm) and for removal of surficial hydrocarbon contaminations, the surface was gradually sputtered by a 500 eV Ar⁺ ion beam with a beam current density in the order of $10 \mu\text{A mm}^{-2}$. For the thermogravimetric analysis (TGA), a Netzsch STA 449 F3 thermal analyzer was used. Around 25 mg of the samples were heated in alumina crucibles using two heating steps under flowing N₂ atmosphere. Starting at room temperature, in the first step, the samples were heated to 302 °C with a rate of 20 °C min⁻¹. In the second step, the samples were heated at a much lower rate of 2.5 °C min⁻¹ to 800 °C. Data was corrected with a baseline measurement of an empty crucible. Time-resolved and time-integrated photoluminescence spectra were obtained using a pulsed laser diode (437 nm, PicoQuant LD-440) with approximately 10 pJ on a spot with a diameter of approximately 30 μm , resulting in flux of $\approx 1 \mu\text{J cm}^{-2}$. The repetition rate of the light source was 250 kHz for TR-PL measurements, while 10 MHz were used for the time-integrated

measurements. The polarization of the excitation was controlled using a Glan–Taylor polarizer and set to s-polarization. Fluorescence of the samples was collected using a Cassegrain-type collection optic (Anagrain; Anaspec Research Laboratories Ltd., Berkshire, UK) in 180° back-scattering geometry, passed through a long-pass filter (458 nm), a wire-grid polarizer (Thorlabs, WP25M-UB) at magic angle with respect to the excitation, and focused onto a fiber/fiber-bundle using an achromatic lens (Thorlabs, AC254-100-AB). For TR-PL experiments, a Triax-190 (Horiba) imaging spectrograph with a 150 lines mm⁻¹ grating ($\lambda_{\text{blaze}} = 500$ nm) was used to disperse the fluorescence coming from the multimode fiber ($\varnothing = 200 \mu\text{m}$, NA 0.12, CeramOptec). For all samples, a central detection wavelength of 650 nm (≈ 1.91 eV) and a bandpass of ≈ 10 nm was used. The spectrograph was focused on a single-photon avalanche diode (Micro Photon Devices, MPD-100-CTE) with the help of an elliptic mirror (Horiba, 1427C). Time-correlated single-photon counting was established using a PicoHarp-300 (PicoQuant). The single-photon timing events were collected in time-tagged time-resolved (TTTR) mode. For time-integrated emission spectra, an Andor Shamrock 163 spectrograph with a 150 lines mm⁻¹ grating ($\lambda_{\text{blaze}} = 500$ nm) was used to disperse the fluorescence coming from a fiber bundle. The spectrally dispersed light was detected utilizing an intensified charged-coupled device camera (iStar720, Andor).

3. Results

To verify the double-perovskite structure and to check for possible secondary phases, Raman spectroscopy was performed.^[26] Figure 2a shows the Raman spectra of the crystals synthesized by solution cooling and microwave-assisted hydrothermal synthesis. Cs₂AgBiBr₆ is known to exhibit characteristic bands with a Raman shift of 75, 135, and 175 cm⁻¹.^[24,27] For both synthesis methods, single-phase Cs₂AgBiBr₆ is formed for Bi25, Bi33, and Bi50 samples. In contrast, Cs₃Bi₂Br₉ is obtained for Bi66 and Bi75 samples where the Raman bands at 190 and 166 cm⁻¹ belong to the stretching vibration modes of the (BiBr₆)³⁻ octahedra in Cs₃Bi₂Br₉.^[28] For MH_Bi66, a mixture of Cs₂AgBiBr₆ and Cs₃Bi₂Br₉ was found. From this observation, it can be concluded that Ag-rich synthesis conditions are beneficial for the formation of Cs₂AgBiBr₆ while the formation of Cs₃Bi₂Br₉ is suppressed both in the solution cooling method and microwave-assisted hydrothermal synthesis. The hydrothermal method is found to extend the formation region of Cs₂AgBiBr₆ into the direction of a Bi-rich composition (MH_Bi66). The full width half maximum (FWHM) values of the A_{1g} Raman band at 175 cm⁻¹ normalized to the T_{2g} band at 75 cm⁻¹ are depicted in Figure 2b. The more defects and imperfections exist in the samples, the broader the Raman bands become due to the change of the local symmetry. Changes in the vibrational modes by lattice imperfections can therefore be sensitively characterized by Raman spectrometry.^[29] As can be seen in Figure 2b, Cs₂AgBiBr₆ single crystals grown by the hydrothermal method exhibit much broader A_{1g} bands and a decrease of the FWHM with increasing Bi content while almost no change in the A_{1g} bandwidth was found for the solution cooling method. Thus, it can be concluded that increasing defect densities or imperfections occur in crystals

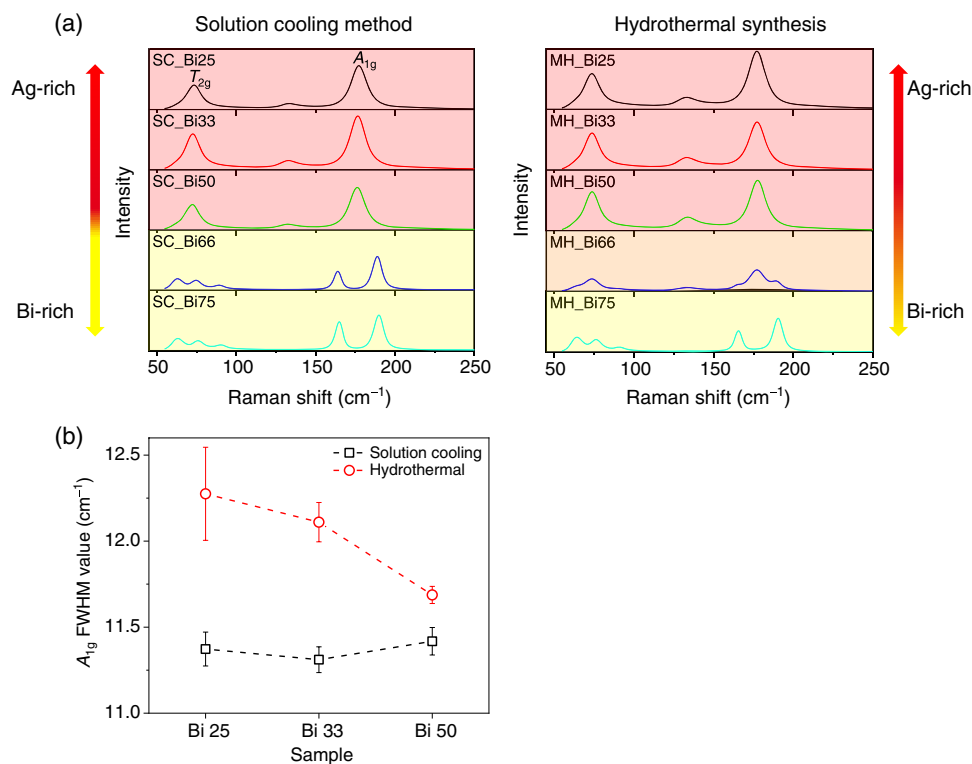


Figure 2. a) Raman spectra of the samples synthesized by solution cooling method and synthesis. The background color red indicates single-phase $\text{Cs}_2\text{AgBiBr}_6$, yellow $\text{Cs}_3\text{Bi}_2\text{Br}_9$, and orange a mixture of both. b) Comparison of full width half maximum (FWHM) values of the A_{1g} band of the obtained $\text{Cs}_2\text{AgBiBr}_6$ single crystals.

synthesized by the hydrothermal method and that the defects are more significant for Ag-rich conditions (MH_Bi25).

The details of the shape, size, and surface roughness of the synthesized single crystals are shown in **Figure 3**. SEM images clearly revealed a well-defined triangular shape of $\text{Cs}_2\text{AgBiBr}_6$ in Bi25, Bi30, and Bi50 for both solution cooling method and the hydrothermal synthesis. The cooling rate in the hydrothermal synthesis is much faster than that in the solution cooling, resulting in much smaller crystals of 10–50 μm compared to the solution cooling method with a size of 100–500 μm . Regarding the compositions of Bi66 and Bi75, the optical microscope images are shown in Figure S2, Supporting Information. The surface of the crystals is rather irregular but sharp by the solution cooling method, while the crystals are round and yellowish by the hydrothermal synthesis.

For a more detailed structure characterization, single-crystal XRD was performed. Phase pure $\text{Cs}_2\text{AgBiBr}_6$ single crystals confirmed by Raman spectroscopy analysis, namely Bi25, Bi30, and Bi50 for both solution cooling and hydrothermal synthesis, were investigated. All measured samples were found to be cubic $\text{Cs}_2\text{AgBiBr}_6$ (space group: $Fm\bar{3}m$). The refined unit cell parameters are plotted in **Figure 4a** and for both synthesis methods they slightly increase with increasing Bi amount up to Bi50. The lattice parameters of $\text{Cs}_2\text{AgBiBr}_6$ grown via the hydrothermal method were larger than those synthesized by the solution cooling. The obtained lattice parameters for the solution cooling method match well with previously reported values in

literature.^[3,17,24,30–33] The lattice expansion of $\text{Cs}_2\text{AgBiBr}_6$ crystals from the hydrothermal method can be interpreted as being caused by significant amounts of defects in the lattice. To investigate the formation of $\text{Ag}_{\text{Bi}}^{\prime\prime}$ antisite defects, the intensity ratios of the (111) and (022) reflections were determined and the results are shown in Figure 4b. A higher ordering is reported to lead to a larger intensity ratio of $I_{(111)}/I_{(022)}$.^[22,34] The samples grown by the hydrothermal method clearly show a decrease of the $I_{(111)}/I_{(022)}$ ratio with decreasing Ag/Bi ratio while the samples obtained from the solution cooling method show minute changes. This indicates that the arrangement of Ag and Bi octahedra was more ordered for the Ag-richer synthesis conditions in the hydrothermal method. Moreover, the amounts of $\text{Ag}_{\text{Bi}}^{\prime\prime}$ antisite defects were profoundly higher for $\text{Cs}_2\text{AgBiBr}_6$ synthesized by the hydrothermal method, especially for the lower Ag/Bi ratio samples. More results of the single-crystal XRD investigations are given in Table S3, Supporting Information.

The ordering degree of Ag and Bi octahedra in the double perovskite structure is reported to affect the bandgap,^[21,25] which was further investigated by UV–vis spectroscopy. **Figure 5** shows the UV–vis diffuse reflectance spectra as a function of wavelength. The varying Ag/Bi ratio does not lead to a significant change in the absorption edge except for MH_Bi50. The obtained absorption edge wavelength of $\text{Cs}_2\text{AgBiBr}_6$ is approximately 600 nm (2.07 eV), which is in good agreement with the reported value.^[27] Above the absorption edge at ≈ 600 nm, a characteristic absorption peak at ≈ 440 nm (2.82 eV) was also observed for both

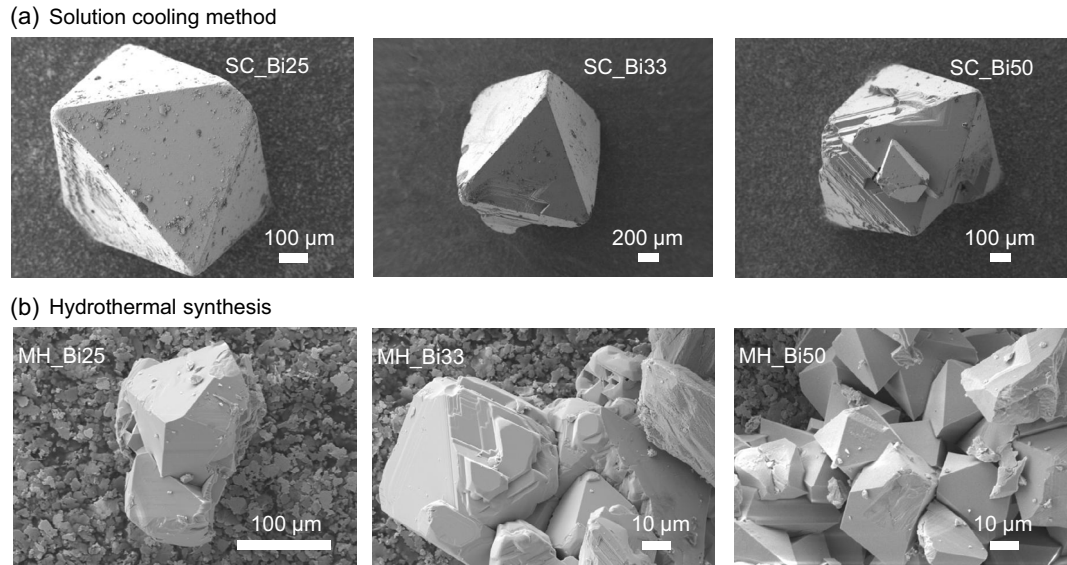


Figure 3. Scanning electron microscope (SEM) images of $\text{Cs}_2\text{AgBiBr}_6$ single crystals synthesized by a) solution cooling method and b) hydrothermal synthesis.

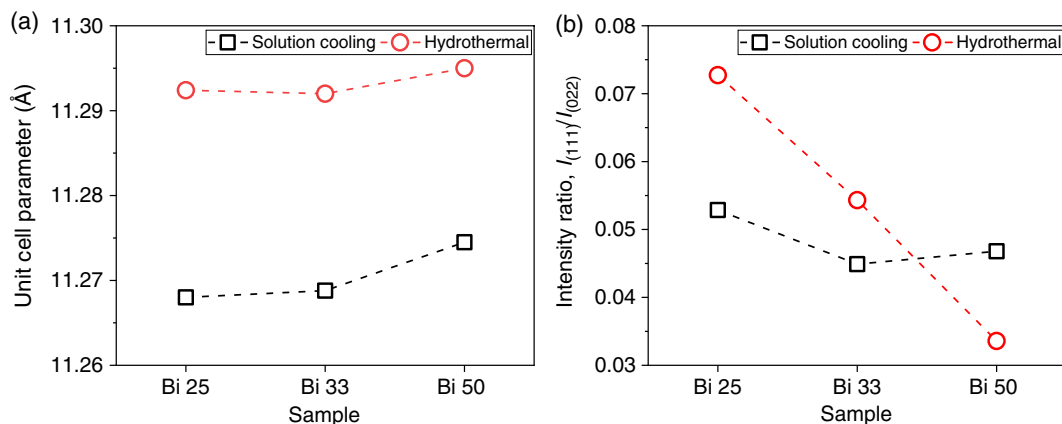


Figure 4. a) Unit cell parameters and b) intensity ratio of the (111) and (022) reflections for the different single crystals.

solution cooling and hydrothermal synthesis, whose peak shape varied depending on the synthesis route. This observation is in a good agreement with the reported direct band to band transition of ≈ 2.8 eV at the Γ point in $\text{Cs}_2\text{AgBiBr}_6$.^[27] However, at the same time, this peak can also be assigned to the excitonic absorption while its origin remains unclear.^[35] $\text{Cs}_2\text{AgBiBr}_6$ is reported to have an indirect bandgap^[36] and thus the Tauc plot assuming an indirect bandgap is also plotted and discussed in Figure S4, Supporting Information.

The exponential decay at the low-energy side of the absorption edge was analyzed for the determination of the Urbach energy as shown in the inset of Figure 5. The Urbach energy of the solution cooling samples was determined to be in the range of $0.071 \text{ eV} \leq E_U \leq 0.089 \text{ eV}$ whilst for the hydrothermally synthesized samples the obtained values are in the range of $0.081 \text{ eV} \leq E_U \leq 0.135 \text{ eV}$. It should also be noted that $\text{Cs}_2\text{AgBiBr}_6$ single crystals grown by the hydrothermal method

exhibited gradual changes of the Urbach energy whereas almost no change was found for the samples synthesized by the solution cooling method. This difference in the synthesis condition resulted in a significant change in the type and total amount of defects in $\text{Cs}_2\text{AgBiBr}_6$. As shown in Figure 1, fast cooling rate was applied to the hydrothermal synthesis compared to the solution cooling method. In addition, the applied pressure might play a role in the hydrothermal method. Contrarily, the solution cooling method was performed under atmospheric pressure. The underlying differences in the nucleation and growth mechanism are not yet fully understood and remain to be elucidated. The observed trends of the Urbach energies are in good accordance with the analysis of the Raman bandwidth shown in Figure 2b. In other words, the change in the Urbach energy was found to be in direct correlation to the broadening of the measured Raman band. This correlation between Urbach energy and Raman line-width was previously reported in the $\text{Mg}_x\text{Zn}_{1-x}\text{O}$ solid solution

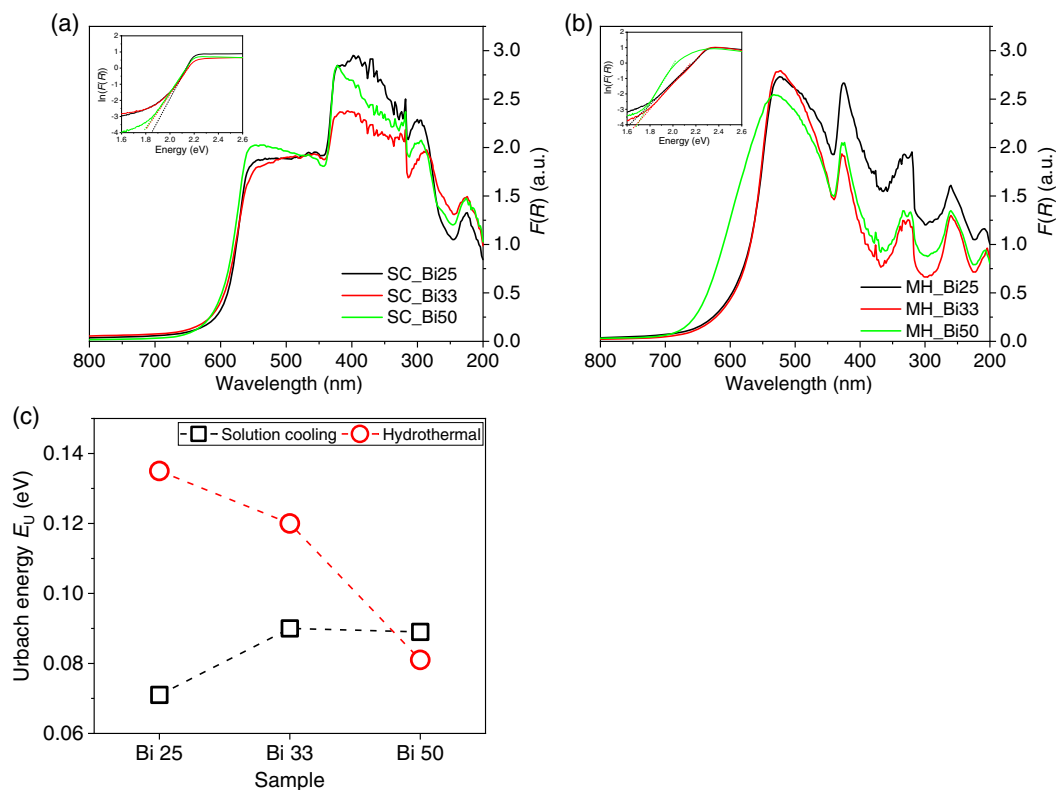


Figure 5. UV-vis diffuse reflectance spectra converted to the Kubelka–Munk function $F(R)$ and logarithmic plot of the absorbance with linear fit for the determination of the Urbach energy E_U of $\text{Cs}_2\text{AgBiBr}_6$ (as illustrated in the inset) for a) solution cooling and b) hydrothermal synthesis. c) The comparison of the obtained Urbach energies is plotted.

by J. Huso et al.,^[37] but to our knowledge, this is the first time that this effect is reported for $\text{Cs}_2\text{AgBiBr}_6$ prepared by different routes. This correlation is also in good agreement with our observations in the XPS measurements.

To detect differences in the defect formation and compositional changes in the synthesized $\text{Cs}_2\text{AgBiBr}_6$ single crystals from both synthesis routes, XPS was carried out. The obtained stoichiometry is shown in Figure 6. The elemental composition of the surface (up to a depth of only a few nanometers) was calculated from the survey spectra by considering the Cs 3*d*, Ag 3*d*, Bi 4*f*, and Br 3*p* peaks and by employing instrument-specific relative sensitivity factors (RSFs). Interestingly, a surplus of Ag to Bi was observed in all the samples except SC_Bi50 as shown in Figure 6a. The Ag surplus is decreasing with decreasing Ag/Bi ratio for the solution cooling method, but for the hydrothermal method, the ratio was almost constant. While SC_Bi33 was nearly stoichiometric, SC_Bi50 exhibited Ag deficiencies that can be interpreted by a possible formation of Ag vacancies. Furthermore, SC_Bi25 showed a clear surplus of Ag to Bi. The XPS spectra collected after a shorter sputtering time, corresponding to a removal of about 2–5 nm of the outermost atomic layers depicted in Figure S5a, Supporting Information, revealed a marked surplus of Ag compared to the results shown in Figure 5. This can be an indication of residual AgBr on the crystal surface, and by TGA, the presence of AgBr was indeed proven in all samples (Figure 7). A similar trend was found for the

(Ag + Bi)/Br ratio as shown in Figure 6b, and it should be mentioned that it is hard to judge which one is the exception out of three samples. It was also noted that the Cs/Br ratio estimated by XPS decreases with decreasing Ag/Bi ratio during the synthesis with exception for MH_Bi33 as shown in Figure 6c. The differentiated Cs/Br ratio between the two synthesis methods is in good agreement with the lattice parameter change determined by single-crystal XRD. The indicative Cs deficiency for solution cooled single crystals found by XPS leads to a shrinkage of the crystal lattice as reported in literature.^[38] The calculated compositions for both synthesis methods showed a surplus of Ag except for SC_Bi50. Considering the Cs/Br ratio obtained, this reveals a substantial amount of Br vacancies. Due to the charging effect, further investigation of the electronic valence states by ultraviolet photoelectron spectroscopy could not be analyzed. Nevertheless, the valence band of the solution cooled samples could be observed with orders of magnitude lower intensity as shown in Figure S5b, Supporting Information. A detectable difference in the valence onset could not be detected within the measurement uncertainty margin for all solution cooling samples.

The thermal stability and the decomposition temperature of the $\text{Cs}_2\text{AgBiBr}_6$ single crystals were investigated by TGA. The mass change, differential thermal gravimetry (DTG) profile, and differential thermal analysis (DTA) curves are shown in

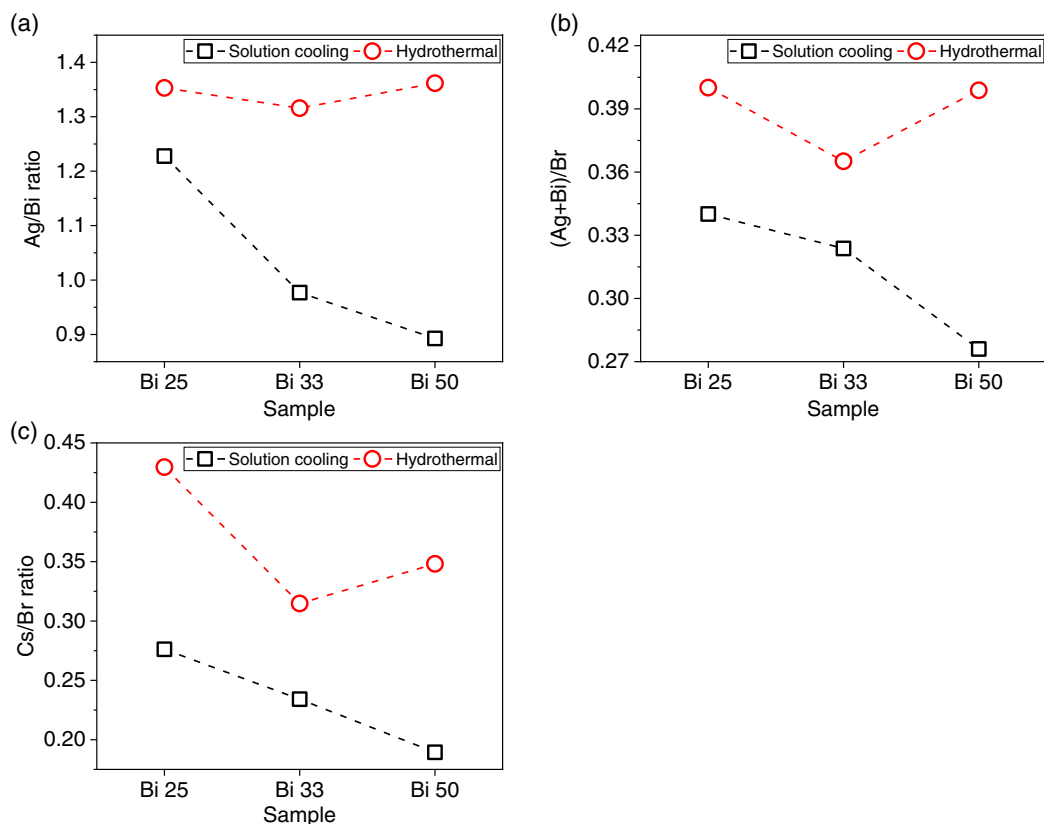


Figure 6. Atomic ratios of a) Ag/Bi, b) (Ag + Bi)Br, and c) Cs/Br determined by X-ray photoelectron spectroscopy (XPS).

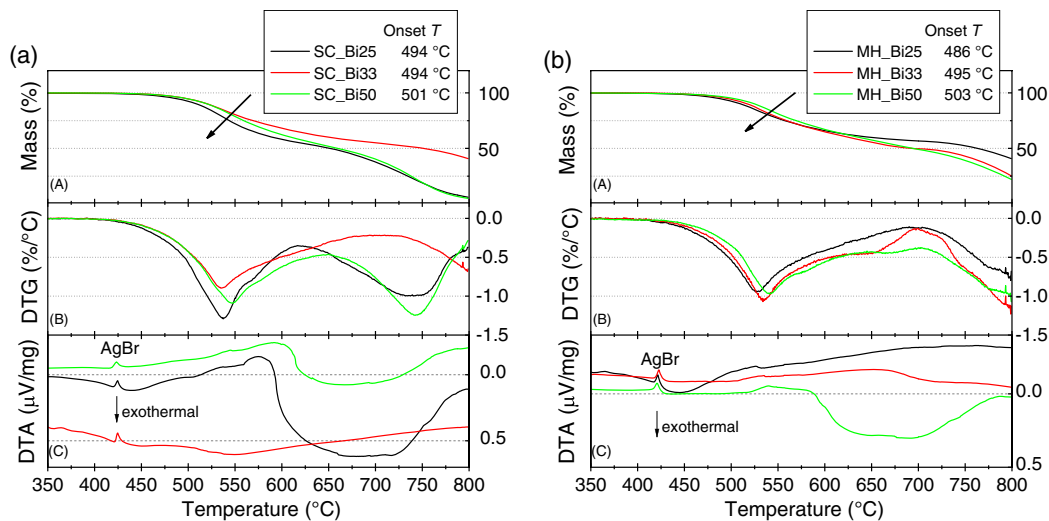


Figure 7. Thermogravimetric analysis (TGA), differential thermal gravimetry (DTG), and differential thermal analysis (DTA) curves of Cs₂AgBiBr₆ synthesized by a) solution cooling and b) hydrothermal synthesis.

Figure 7. The decomposition temperature was determined from the onset temperature (tangent method) of the TG curve. Samples from both the solution cooling and the hydrothermal synthesis exhibited a similar onset of 501 and 503 °C, respectively, for the same precursor stoichiometry of Bi50. This is in the same range as the reported decomposition temperature,^[33]

which can be controlled by varying the Ag/Bi ratio during synthesis. For the solution cooling method, Bi33 and Bi25 exhibited a decomposition temperature of 494 °C, which is lower than that of Bi50. Decomposition temperatures of 495 and 486 °C were obtained for Bi33 and Bi25, respectively, for the hydrothermal synthesis, indicating that in both synthesis methods, the

decomposition temperature decreases upon increasing the Ag/Bi ratio. For SC_Bi50 and SC_Bi25, the position of the minimum value in the DTG is found to be at 547 and 537 °C, respectively. For MH_Bi50 and MH_Bi25, the position of the minimum value in the DTG is found to be at 541 and 526 °C, respectively. Interestingly, in the DTA curve, a small endothermic peak at ≈ 424 °C was observed for all samples. This corresponds to be the melting point of AgBr,^[39] indicating the existence of AgBr on the surface of the Cs₂AgBiBr₆ single crystals, as confirmed by XPS analysis with varied sputtering time. The decreasing decomposition temperature with increasing Ag/Bi ratio follows the same trend as the broadening of the Raman band and the Urbach energy, especially for the hydrothermally synthesized samples. Thus, the decreased decomposition temperature can be regarded as an indicator for the crystal imperfection. The generated defects decrease the decomposition enthalpy, so that a lower temperature is needed for the chemical decomposition. By evaluation of the calculated decomposition energy, Cs₂AgBiBr₆ has been reported to decompose into AgBr, CsAgBr₂, and Cs₃Bi₂Br₉.^[20]

To obtain a better understanding of the photoexcitation and photoemission characteristics of Cs₂AgBiBr₆, we have performed PL spectroscopy. The PL spectra for the different samples from the two synthesis routes are presented in **Figure 8**. All samples reveal an emission peak at 1.9 eV, which is Stokes-shifted compared to the UV–vis absorption onset. This is in good agreement with the reported literature values between 1.9 and 1.95 eV for Cs₂AgBiBr₆ single crystals.^[13,14,18,27,40,41] Compared to the estimated bandgap from UV–vis diffuse reflectance spectra, it is interestingly found that no significant or fundamental difference occurs in the position of the emission peak for the samples synthesized via both synthesis routes. It should be noted that the shape of the emission peak is strongly asymmetric and broad. The origin of asymmetric spectra shape and broadness is ascribed to the contributions from indirect band to band transition, the electron–phonon coupling, and the lower energy emission due to the defect states in the band structure or self-trapped excitons (STEs).^[35] The lifetime of charge carriers was obtained by TR-PL at the band-edge emission of 1.9 eV with an excitation energy of 2.8 eV. The decay curves were fitted with a double exponential decay equation (Equation (3)).

$$I(t) = A_1 \exp\left(\frac{-t}{\tau_1}\right) + A_2 \exp\left(\frac{-t}{\tau_2}\right) \quad (3)$$

where t is the time, A_1 and A_2 are pre-exponential factors, and τ_1 and τ_2 are the corresponding decay times for the exponential components, respectively. The fitting results of decay profiles are presented in **Figure 9**. The crystals synthesized by the solution cooling method do not show a significant difference for the varied Ag/Bi precursor ratios. However, for the hydrothermally synthesized crystals, the results clearly show a significant difference of the decay profiles with changing Ag/Bi ratio. The samples synthesized at a higher Ag/Br precursor ratio showed a longer decay time than those synthesized under stoichiometric Ag/Br synthesis condition. The decay constants are ranging from 1 to 3 ns for τ_1 and from 11 to 23 ns for τ_2 . Here, τ_1 is found to be in the range described in literature, but τ_2 seems to be much smaller than reported by M. Keshavarz et al.^[41] As discussed by Slavney et al. and other research groups, the short and intermediate time decay should be highly correlated to defects as charge trapping centers.^[13,18,36,41,42] In contrast, the interpretation of time-resolved studies is still under debate and our findings concerning the change in the intermediate decay τ_2 will be further studied. Nevertheless, for the solution cooling samples, the decay constant τ_1 differed only marginally within the estimated measurement error range and just a slight change in τ_2 was observed. In contrast, for Cs₂AgBiBr₆ crystals prepared by the hydrothermal method both decay constants τ_1 and τ_2 vary with the Ag/Bi precursor ratio of the precursor solutions.

4. Discussion

In this study, the type and concentration of defects as well as the formation of the secondary-phase Cs₃Bi₂Br₉ were found to be strongly dependent on the precursor Ag/Bi ratio and the different synthetic routes. Applying Ag-rich conditions during the synthesis was favorable for preventing the formation of Cs₃Bi₂Br₉. In contrast, a Bi-rich synthesis condition was not favorable for obtaining single-phase Cs₂AgBiBr₆ for both the solution cooling method and the hydrothermal method. By applying various characterization techniques, Cs₂AgBiBr₆ single

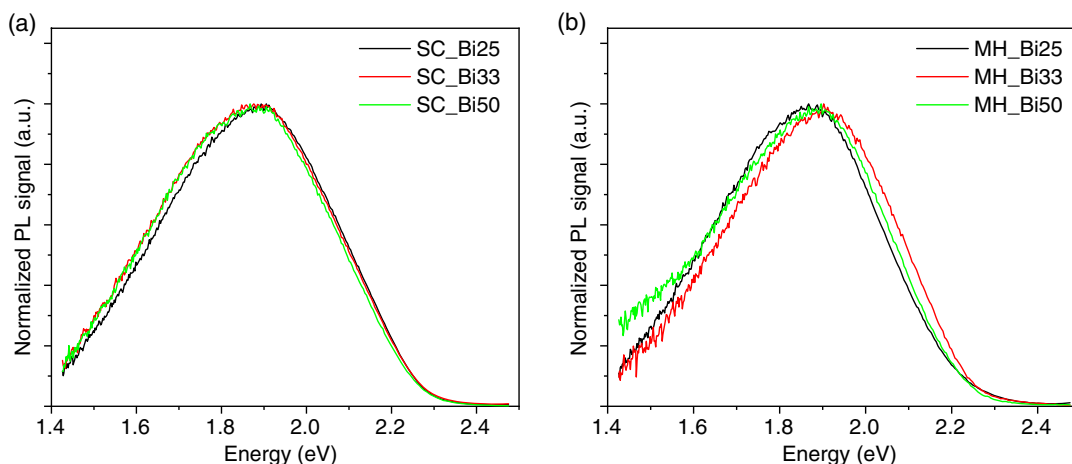


Figure 8. Photoluminescence (PL) spectra of Cs₂AgBiBr₆ synthesized by a) solution cooling and b) hydrothermal synthesis.

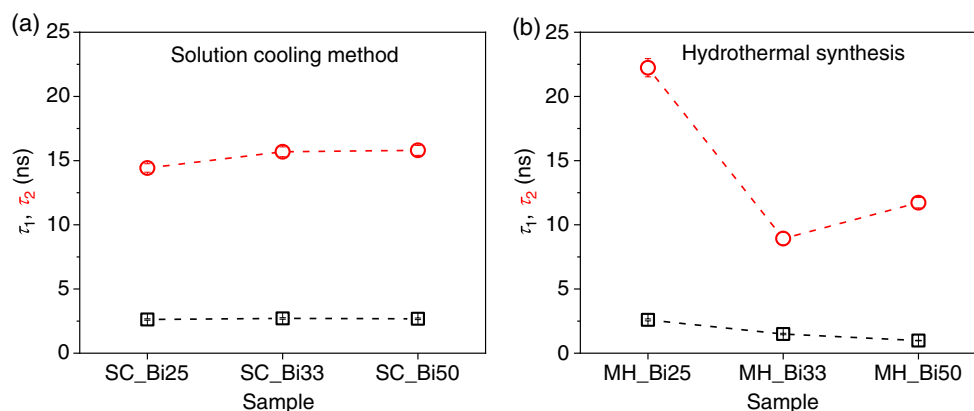


Figure 9. Determined decay parameters τ_1 and τ_2 from time-resolved photoluminescence (TR-PL) of the samples prepared by a) solution cooling method and b) hydrothermal synthesis.

crystals were thoroughly investigated. The tendency observed in TR-PL was in good agreement with the Raman band broadening and the estimated Urbach energy values from UV-vis spectroscopy. Single crystals synthesized by the solution cooling method showed no significant band broadening in Raman spectroscopy, smaller cell parameters, negligible change both in absorption edge shift and Urbach energy, and finally no dramatic change in the decay constant in TR-PL. In contrast, in hydrothermally synthesized $\text{Cs}_2\text{AgBiBr}_6$, the increase of the Raman broadening and the Urbach energy indirectly reveals higher amounts of defects. Lower Bi content leads to the formation of Ag vacancies or Ag_{Bi}'' antisite defects to meet the charge neutrality. Furthermore, significantly more Br vacancies were found in the hydrothermal synthesis compared to the solution cooling method. Generally, high amounts of defects would result in a decrease of the carrier lifetime. According to Xiao et al.,^[20] however, the energy level position of Br vacancies was calculated to be placed 0.03 eV below the conduction band within the bandgap. Hence, Br vacancies could be shallow electron traps that increase the charge-carrier lifetime as schematically shown in **Figure 10**. Here, two mechanisms of charge trapping are plausible. First, directly after photoexcitation, trapping and detrapping of the excited electrons can happen within 10 ps during photon-assisted

transfer to the bottom of the conduction band by electron intervalley scattering.^[14] Second, after the electron intervalley scattering, the electrons can be trapped and detrapped at shallow stable defects formed by Br vacancies close to the bottom of the conduction band. Further investigations, for example, picosecond time-resolved spectroscopy will shed light on this topic.

Ahn et al. reported that Ag-rich conditions in the initial chemical environments not only suppress the formation of Ag vacancies, but also prevent the formation of the secondary-phase $\text{Cs}_3\text{Bi}_2\text{Br}_9$ in hydrothermal synthesis.^[17] In contrast to their report, in our study, $\text{Cs}_2\text{AgBiBr}_6$ single crystals grown from Ag-rich precursor solutions revealed Ag vacancies together with Br vacancies. It should be noted that the range of initial molar concentrations of Ag^+ and Bi^{3+} investigated in our study ($\pm 300\%$ from stoichiometric $\text{Ag}^+/\text{Bi}^{3+}$ ratio) is much wider than the compositional range reported by Ahn et al. ($\pm 20\%$ from stoichiometric $\text{Ag}^+/\text{Bi}^{3+}$ ratio). Our results are in good line with previous reports in the respect that the precise tuning of stoichiometry of synthesized $\text{Cs}_2\text{AgBiBr}_6$ can have a direct impact on the optical properties.^[17–19]

The absorption spectra used for the Urbach energy estimation revealed that hydrothermally synthesized $\text{Cs}_2\text{AgBiBr}_6$ single crystals can be fitted with two single exponentials whereas the

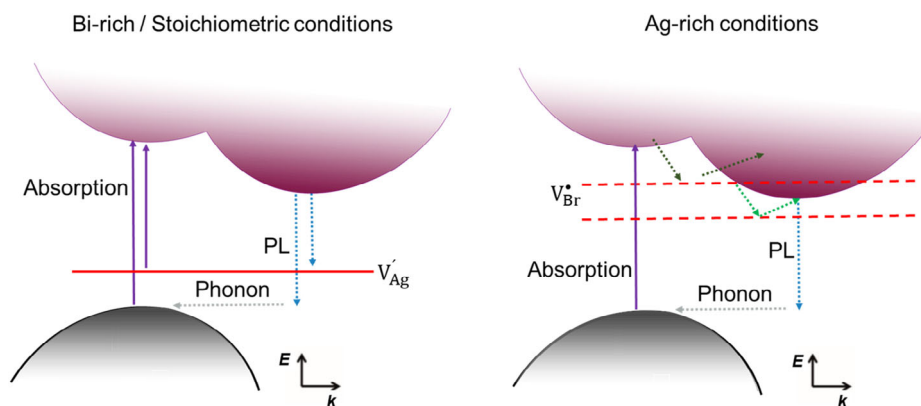


Figure 10. Schematic illustration of the induced dominant defects for Bi-rich/stoichiometric conditions and Ag-rich conditions. Light absorption, emission, and trapping/detrapping mechanisms of charge carriers are highlighted.

data for solution cooling samples can be well fitted by one exponential function. We cannot rule out the possibility that the samples synthesized by the hydrothermal synthesis may contain another type of non-negligible defects in addition to Br vacancies. This issue needs further investigations. A possible explanation for our observation can be the formation of Ag vacancies or antisite defects Ag_{Bi}'' , both of which can play a role as a hole trap. Formation of Ag vacancies in Ag-rich conditions seems not likely. Instead, if antisite Ag_{Bi}'' defects are more favorably formed in the hydrothermal method together with Br vacancies, the larger Urbach energy and increased carrier lifetime can be satisfactorily explained. The change in Urbach energy might also show up in the change of peak broadening in PL emission spectroscopy. For instance, Lei et al. have shown that asymmetric PL spectra of $\text{Cs}_2\text{AgBiBr}_6$ can be deconvoluted by band-to-band transition and defects-related excitons or STE.^[35] Steele et al. argued that Urbach tail from sub-bandgap defects was clearly observed in PL emission spectroscopy.^[43] However, the PL emission signals were too broad to be accurately analyzed in our study. The defects and their role in the synthesis and characterization of $\text{Cs}_2\text{AgBiBr}_6$ single crystals are particularly important, yet poorly defined indicators. One remaining question is why more Br vacancies and Ag_{Bi}'' antisite defects can be formed in hydrothermally synthesized samples compared to the solution cooling method. As an outlook, it is anticipated to calculate the change of band structure, depending on the defects type and concentration. The degree of bandgap narrowing with controlled defect concentration is an interesting topic. The significance of each defect type such as Br vacancy, Ag vacancy, and antisite defect Ag_{Bi}'' on the bandgap in $\text{Cs}_2\text{AgBiBr}_6$ needs to be investigated further.

5. Summary

$\text{Cs}_2\text{AgBiBr}_6$ single crystals were synthesized by the solution cooling method and the hydrothermal synthesis. Under controlled $\text{Ag}^+/\text{Bi}^{3+}$ ratio during the synthesis, the defect type and concentration in resulting $\text{Cs}_2\text{AgBiBr}_6$ single crystals were successfully varied. The crystal structure, composition, thermal stability, and optical properties were investigated. From the estimated band broadening analysis in Raman spectroscopy and Urbach energy by UV-vis spectroscopy, it is confirmed that the defect concentration is changed by a variation of the Ag/Bi ratio in the precursor solutions. It could be confirmed that Ag-rich synthesis conditions prevent the formation of $\text{Cs}_3\text{Bi}_2\text{Br}_9$, but an increasing Ag concentration induces the generation of Br vacancies. This formation of Br vacancies results in pronounced trapping-assisted recombination processes leading to a longer carrier lifetime. Based on our findings, the synthesis conditions for achieving higher PCE in $\text{Cs}_2\text{AgBiBr}_6$ -based thin-film solar cells are rationalized.

Supporting Information

Supporting Information is available from the Wiley Online Library or from the author.

Acknowledgements

This work was financially supported by Fraunhofer Lighthouse Project MaNiTU—Materials for sustainable tandem solar cells with extremely high conversion efficiency. Open access funding has been enabled and organized by Fraunhofer-Gesellschaft.

Open Access funding enabled and organized by Projekt DEAL.

Conflict of Interest

The authors declare no conflict of interest.

Data Availability Statement

The data that support the findings of this study are available from the corresponding author upon reasonable request.

Keywords

$\text{Cs}_2\text{AgBiBr}_6$, defects, Raman spectroscopy, time-resolved photoluminescence, urbach energy

Received: March 1, 2022

Revised: May 13, 2022

Published online:

- [1] A. Babayigit, A. Ethirajan, M. Muller, B. Conings, *Nat. Mater.* **2016**, *15*, 247.
- [2] M. A. Green, A. Ho-Baillie, H. J. Snaith, *Nat. Photonics* **2014**, *8*, 506.
- [3] E. T. McClure, M. R. Ball, W. Windl, P. M. Woodward, *Chem. Mater.* **2016**, *28*, 1348.
- [4] M. R. Filip, S. Hillman, A. A. Haghighirad, H. J. Snaith, F. Giustino, *J. Phys. Chem. Lett.* **2016**, *7*, 2579.
- [5] W. Pan, H. Wu, J. Luo, Z. Deng, C. Ge, C. Chen, X. Jiang, W.-J. Yin, G. Niu, L. Zhu, L. Yin, Y. Zhou, Q. Xie, X. Ke, M. Sui, J. Tang, *Nat. Photonics* **2017**, *11*, 726.
- [6] M. T. Sirtl, F. Ebadi, B. T. Gorkom, P. Ganswindt, R. A. J. Janssen, T. Bein, W. Tress, *Adv. Opt. Mater.* **2021**, *9*, 2100202.
- [7] W. Tress, M. T. Sirtl, *Sol. RRL* **2022**, *6*, 2100770.
- [8] B. Wang, N. Li, L. Yang, C. Dall'Agnesse, A. K. Jena, S.-I. Sasaki, T. Miyasaka, H. Tamiaki, X.-F. Wang, *J. Am. Chem. Soc.* **2021**, *143*, 2207.
- [9] K.-Z. Du, W. Meng, X. Wang, Y. Yan, D. B. Mitzi, *Angew. Chem., Int. Ed.* **2017**, *56*, 8158.
- [10] G. Volonakis, M. R. Filip, A. A. Haghighirad, N. Sakai, B. Wenger, H. J. Snaith, F. Giustino, *J. Phys. Chem. Lett.* **2016**, *7*, 1254.
- [11] A. Karmakar, M. S. Dodd, S. Agnihotri, E. Ravera, V. K. Michaelis, *Chem. Mater.* **2018**, *30*, 8280.
- [12] Y. Yin, W. Tian, J. Leng, J. Bian, S. Jin, *J. Phys. Chem. Lett.* **2020**, *11*, 6956.
- [13] A. D. Wright, L. R. V. Buizza, K. J. Savill, G. Longo, H. J. Snaith, M. B. Johnston, L. M. Herz, *J. Phys. Chem. Lett.* **2021**, *12*, 3352.
- [14] A. Dey, A. F. Richter, T. Debnath, H. Huang, L. Polavarapu, J. Feldmann, *ACS nano* **2020**, *14*, 5855.
- [15] G. Longo, S. Mahesh, L. R. V. Buizza, A. D. Wright, A. J. Ramadan, M. Abdi-Jalebi, P. K. Nayak, L. M. Herz, H. J. Snaith, *ACS Energy Lett.* **2020**, *5*, 2200.
- [16] V. M. Caselli, Z. Wei, M. M. Ackermans, E. M. Hutter, B. Ehrler, T. J. Savenije, *ACS Energy Lett.* **2020**, *5*, 3821.

- [17] C. W. Ahn, J. H. Jo, J. Chan Kim, H. Ullah, S. Ryu, Y. Hwang, J. San Choi, J. Lee, S. Lee, H. Jeon, Y.-H. Shin, H. Y. Jeong, I. W. Kim, T. H. Kim, *J. Materiomics* **2020**, *6*, 651.
- [18] M. T. Sirtl, M. Armer, L. K. Reb, R. Hooijer, P. Dörflinger, M. A. Scheel, K. Tvingstedt, P. Rieder, N. Glück, P. Pandit, S. V. Roth, P. Müller-Buschbaum, V. Dyakonov, T. Bein, *ACS Appl. Energy Mater.* **2020**, *3*, 11597.
- [19] Z. Zhang, D. Cao, Z. Huang, E. O. Danilov, C.-C. Chung, D. Sun, G. Yang, *Adv. Optical Mater.* **2021**.
- [20] Z. Xiao, W. Meng, J. Wang, Y. Yan, *ChemSusChem* **2016**, *9*, 2628.
- [21] J. Yang, P. Zhang, S.-H. Wei, *J. Phys. Chem. Lett.* **2018**, *9*, 31.
- [22] W. Yuan, G. Niu, Y. Xian, H. Wu, H. Wang, H. Yin, P. Liu, W. Li, J. Fan, *Adv. Funct. Mater.* **2019**, *29*, 1900234.
- [23] P. Kubelka, F. Munk, *Z. Phys. Chem.* **1931**, *12*, 593.
- [24] J. A. Steele, P. Puech, M. Keshavarz, R. Yang, S. Banerjee, E. Debroye, C. W. Kim, H. Yuan, N. H. Heo, J. Vanacken, A. Walsh, J. Hofkens, M. B. J. Roeffaers, *ACS nano* **2018**, *12*, 8081.
- [25] F. Urbach, *Phys. Rev.* **1953**, *92*, 1324.
- [26] P. Pistor, M. Meyns, M. Guc, H.-C. Wang, M. A. L. Marques, X. Alcobé, A. Cabot, V. Izquierdo-Roca, *Scr. Mater.* **2020**, *184*, 24.
- [27] S. J. Zelewski, J. M. Urban, A. Surrente, D. K. Maude, A. Kuc, L. Schade, R. D. Johnson, M. Dollmann, P. K. Nayak, H. J. Snaith, P. Radaelli, R. Kudrawiec, R. J. Nicholas, P. Plochocka, M. Baranowski, *J. Mater. Chem. C* **2019**, *7*, 8350.
- [28] G. Bator, J. Bara, R. Jakubas, M. Karbowski, *Vib. Spectrosc.* **1998**, *16*, 11.
- [29] G. Gouadec, P. Colomban, *Prog. Cryst. Growth Charact. Mater.* **2007**, *53*, 1.
- [30] F. Ji, J. Klarbring, F. Wang, W. Ning, L. Wang, C. Yin, J. S. M. Figueroa, C. K. Christensen, M. Etter, T. Ederth, L. Sun, S. I. Simak, I. A. Abrikosov, F. Gao, *Angew. Chem., Int. Ed.* **2020**, *59*, 15191.
- [31] A. H. Slavney, T. Hu, A. M. Lindenberg, H. I. Karunadasa, *J. Am. Chem. Soc.* **2016**, *138*, 2138.
- [32] W. Ning, X.-G. Zhao, J. Klarbring, S. Bai, F. Ji, F. Wang, S. I. Simak, Y. Tao, X.-M. Ren, L. Zhang, W. Huang, I. A. Abrikosov, F. Gao, *Adv. Funct. Mater.* **2019**, *29*, 1807375.
- [33] J. Su, Y. Huang, H. Chen, J. Huang, *Cryst. Res. Technol.* **2020**, *55*, 1900222.
- [34] N. Setter, L. E. Cross, *J. Mater. Sci.* **1980**, *15*, 2478.
- [35] H. Lei, D. Hardy, F. Gao, *Adv. Funct. Mater.* **2021**, *31*, 2105898.
- [36] A. H. Slavney, L. Leppert, D. Bartesaghi, A. Gold-Parker, M. F. Toney, T. J. Savenije, J. B. Neaton, H. I. Karunadasa, *J. Am. Chem. Soc.* **2017**, *139*, 5015.
- [37] J. Huso, H. Che, D. Thapa, A. Canul, M. D. McCluskey, L. Bergman, *J. Appl. Phys.* **2015**, *117*, 125702.
- [38] H. Chen, C.-R. Zhang, Z.-J. Liu, J.-J. Gong, W. Wang, Y.-Z. Wu, H.-S. Chen, *Mater. Sci. Semicond. Process* **2021**, *123*, 105541.
- [39] A. Górniak, A. Wojakowska, S. Plińska, E. Krzyżak, *J. Therm. Anal. Calorim.* **2009**, *96*, 133.
- [40] R. L. Z. Hoye, L. Eyre, F. Wei, F. Brivio, A. Sadhanala, S. Sun, W. Li, K. H. L. Zhang, J. L. MacManus-Driscoll, P. D. Bristowe, R. H. Friend, A. K. Cheetham, F. Deschler, *Adv. Mater. Interfaces* **2018**, *5*, 1800464.
- [41] M. Keshavarz, E. Debroye, M. Ottesen, C. Martin, H. Zhang, E. Fron, R. Küchler, J. A. Steele, M. Bremholm, J. van de Vondel, H. I. Wang, M. Bonn, M. B. J. Roeffaers, S. Wiedmann, J. Hofkens, *Adv. Mater.* **2020**, *32*, e2001878.
- [42] L. R. V. Buizza, A. D. Wright, G. Longo, H. C. Sansom, C. Q. Xia, M. J. Rosseinsky, M. B. Johnston, H. J. Snaith, L. M. Herz, *ACS Energy Lett.* **2021**, *6*, 1729.
- [43] J. A. Steele, W. Pan, C. Martin, M. Keshavarz, E. Debroye, H. Yuan, S. Banerjee, E. Fron, D. Jonckheere, C. W. Kim, W. Baekelant, G. Niu, J. Tang, J. Vanacken, M. van der Auweraer, J. Hofkens, M. B. J. Roeffaers, *Adv. Mater.* **2018**, *30*, e1804450.